

Guiding transition metal-doped hollow cerium tandem nanozymes with elaborately regulated multi-enzymatic activities for intensive chemodynamic therapy

Dong, Shuming; Dong, Yushan; Liu, Bin; Liu, Jing; Liu, Shikai; Zhao, Zhiyu; Li, Wenting; Tian, Boshi; Zhao, Ruoxi; He, Fei; Gai, Shili; Xie, Ying; Yang, Piaoping; Zhao, Yanli

2022

Dong, S., Dong, Y., Liu, B., Liu, J., Liu, S., Zhao, Z., Li, W., Tian, B., Zhao, R., He, F., Gai, S., Xie, Y., Yang, P. & Zhao, Y. (2022). Guiding transition metal-doped hollow cerium tandem nanozymes with elaborately regulated multi-enzymatic activities for intensive chemodynamic therapy. *Advanced Materials*, 34(7), 2107054-.
<https://dx.doi.org/10.1002/adma.202107054>

<https://hdl.handle.net/10356/155940>

<https://doi.org/10.1002/adma.202107054>

This is the peer reviewed version of the following article: Dong, S., Dong, Y., Liu, B., Liu, J., Liu, S., Zhao, Z., Li, W., Tian, B., Zhao, R., He, F., Gai, S., Xie, Y., Yang, P. & Zhao, Y. (2022). Guiding transition metal-doped hollow cerium tandem nanozymes with elaborately regulated multi-enzymatic activities for intensive chemodynamic therapy. *Advanced Materials*, 34(7), 2107054, which has been published in final form at <https://doi.org/10.1002/adma.202107054>. This article may be used for non-commercial purposes in accordance with Wiley Terms and Conditions for Use of Self-Archived Versions.

Guiding Transition Metal-Doped Hollow Cerium Tandem Nanozymes with Elaborately Regulated Multi-Enzymatic Activities for Intensive Chemodynamic Therapy

Shuming Dong, Yushan Dong, Bin Liu, Jing Liu, Shikai Liu, Zhiyu Zhao, Wenting Li, Boshi Tian, Ruoxi Zhao, Fei He*, Shili Gai, Ying Xie, Piaoping Yang*, and Yanli Zhao*

S. Dong, Y. Dong, B. Liu, J. Liu, S. Liu, W. Li, B. Tian, R. Zhao, Prof. F. He, S. Gai, Prof. P. Yang
Key Laboratory of Superlight Materials and Surface Technology, Ministry of Education, College of Material Sciences and Chemical Engineering, Harbin Engineering University, Harbin 150001, P. R. China. Email: hefei@hrbeu.edu.cn; yangpiaoping@hrbeu.edu.cn

Prof. Y. L. Zhao

Division of Chemistry and Biological Chemistry, School of Physical and Mathematical Sciences, Nanyang Technological University, 21 Nanyang Link, Singapore 637371, Singapore. Email: zhaoyanli@ntu.edu.sg

Prof. Y. Xie

Key Laboratory of Functional Inorganic Material Chemistry, Ministry of Education, School of Chemistry and Materials Science, Heilongjiang University, Harbin, 150080, P. R. China.

Dr. Z. Zhao

Department of Ultrasound, The First Affiliated Hospital of Harbin Medical University, Harbin 150001, P. R. China.

S. Dong and Y. Dong contributed equally to this work.

Abstract. Clinical applications of nanozyme-initiated chemodynamic therapy (NCDT) have been severely limited by poor catalytic efficiency of nanozymes, insufficient endogenous H_2O_2 content, and off-target consumption. Herein, we develop hollow mesoporous Mn/Zr-co-doped CeO_2 tandem nanozyme (PHMZCO-AT) with elaborately regulated multi-enzymatic activities, i.e., simultaneously enhancing superoxide dismutase (SOD)-like and peroxidase (POD)-like activities and inhibiting catalase (CAT)-like activity, serving as an H_2O_2 homeostasis disruptor to promote H_2O_2 evolution and restrain off-target elimination of H_2O_2 for achieving intensive NCDT.

PHMZCO-AT nanozymes with SOD-like activity can catalyze endogenous $O_2^{\cdot-}$ into H_2O_2 in the tumor region. The suppression of CAT activity and depletion of glutathione by PHMZCO-AT largely weaken the off-target decomposition of H_2O_2 to H_2O . Elevated H_2O_2 is then exclusively catalyzed by the downstream POD-like activity of PHMZCO-AT to generate toxic hydroxyl radicals, further inducing tumor apoptosis and death. T_1 -weighted magnetic resonance imaging and high-contrast X-ray computed tomography imaging are also achieved using PEG/PHMZCO-AT nanozymes due to the existence of paramagnetic Mn^{2+} species and high X-ray attenuation ability of elemental Zr, permitting *in vivo* tracking of the therapeutic process. This work presents a powerful paradigm to achieve intensive NCDT efficacy by simultaneously regulating multi-enzymatic activities of Ce-based nanozymes and perturbing the H_2O_2 homeostasis in tumor microenvironment.

Keywords: cancer treatment, chemodynamic therapy, hollow cerium, homeostasis disruptor, tandem nanozymes

Introduction

For cancers, a mature mechanism in which the redox equilibrium threshold of tumor cells is much higher than that of normal cells and is more sensitive to reactive oxygen species (ROS) level elevations has attracted remarkable attention.^[1] From this perspective, ROS-generating approaches have been widely explored as a weapon to directly or indirectly kill cancer cells, including photodynamic therapy (PDT),^[2] radiodynamic therapy (RT),^[3] sonodynamic therapy (SDT),^[4] and chemodynamic therapy (CDT).^[5] Promoted by recent advancements in nanochemistry and nanocatalysis, a variety of nanosystems with enzyme-like activities, also called “nanozymes”, have been successfully fabricated and applied in various biomedical applications.^[6] Among which, nanozyme-initiated CDT (NCDT), a high tumor-specific modality for cancer therapy triggered by peroxidase (POD)-like nanozyme-mediated chemical reactions, that is, *in situ* catalyzing the endogenous hydrogen peroxide (H_2O_2) into highly toxic hydroxyl radicals ($\cdot OH$) for inducing cell apoptosis and necrosis, is emerging as a novel cancer treatment tactic with the potential to mitigate undesired side effects. Although many nanomaterials, including ferromagnetic nanoparticles (γ - Fe_2O_3 or Fe_3O_4),^[7] vanadium oxides,^[8] copper oxide,^[9] and cerium oxide (CeO_2),^[10] have revealed the POD-like activity for cancer diagnosis and treatment, the one-off and low catalytic performance make them challenging to realize desirable therapeutic efficacy. In general, the POD-like catalytic activity of these metal oxide-based nanozymes depends on low-valent metal ions (e.g., Fe^{2+} , Cu^+ , Mn^{2+} , and Ce^{3+}) just like the Fenton’s reagents which are known to catalyze the disproportionation of H_2O_2 to generate $\cdot OH$ radical.^[11] Taking Fe^{2+} -catalyzed Fenton reaction as an example, Fe^{2+}

with high catalytic activity is inevitably oxidized into Fe^{3+} . Fe^{3+} shows much lower catalytic efficiency compared with Fe^{2+} , and the conversion rate ($0.002\text{--}0.01\text{M}^{-1}\text{ s}^{-1}$) from Fe^{3+} to Fe^{2+} is very slow, which highly retards the POD-like catalytic activity.^[12] Thus, accelerating the transformation of high-valence metal ions into catalytic ones (low-valence) in a sustained manner should be a facile and efficient method to dynamically regulate the POD-like activity of these metal oxide-based nanozymes for improving the therapeutic effect of NCDT.

To better promote the therapeutic efficiency of designed nanozymes, one crucial factor, namely, the tumor microenvironment (TME), should be considered. While the TME characterized by hypoxia, mild acidity, and H_2O_2 production is due to the abnormal metabolism of tumor cells compared to normal cells,^[13] the H_2O_2 level is insufficient to continuously produce $\cdot\text{OH}$ for achieving effective NCDT. Thus, the introduction of an H_2O_2 -evolving capability into NCDT has been widely designed and developed for enhancing their anticancer performance. Strategies include the direct loading of exogenous H_2O_2 or H_2O_2 pro-catalysts (glucose oxidase or metal peroxides) into the tumor site.^[14] However, these approaches are either subjected to safety concerns on account of the premature leakage of cargoes or are impeded by the rapid consumption of metal peroxides. Therefore, it may be a better approach to stimulate *in situ* H_2O_2 generation with the purpose of a specific response and consecutive manner. In addition, it is known that the level of H_2O_2 keeps homeostasis by balancing generation with their elimination by antioxidant systems in the cancer cells, such as superoxide dismutase (SOD), glutathione peroxidase (GPx), and catalase (CAT), as well as antioxidant biomolecules including glutathione (GSH, high intracellular concentration of $10 \times 10^{-3}\text{ M}$).^[15] In detail, the superoxide anions ($\text{O}_2^{\cdot-}$) can be disproportionated to produce H_2O_2 catalyzed by SOD, and the generated H_2O_2 is usually transformed to H_2O by GPx in the presence of GSH, or directly depleted by GSH, as well as catalytically decomposed to O_2 and H_2O by CAT.^[16] Based on these mechanisms, we conceive that breaking the dynamic balance of H_2O_2 by promoting H_2O_2 generation and inhibiting the off-target elimination of H_2O_2 with the designed nanozymes can achieve a high accumulation of H_2O_2 in tumor cells, in which the elevated H_2O_2 content is then exclusively catalyzed by the downstream POD-like nanozymes *via* Fenton-like reactions to liberate highly toxic $\cdot\text{OH}$. However, all-in-one theranostic nanozymes with elaborately regulated multi-enzymatic activities to make the above functions possible have been rarely reported.

Owing to the existence of mixed-valence states of Ce^{3+} and Ce^{4+} , and the existence of oxygen vacancies, CeO_2 displays multiple enzyme-like catalytic activities, including POD-like, CAT-like, and SOD-like activities, showing the potential as nanozymes for biomedical applications due to superior chemical stability, biocompatibility, and very low Ce ion leaching.^[17] However, on account of relatively inert redox cyclability from Ce^{4+} to Ce^{3+} and highly chaotic enzymatic

activities, the therapeutic effect of pure CeO_2 -initiated NCDT is severely limited. Notably, the redox enzyme-mimicking activities of CeO_2 highly depend on the redox state of Ce ions on its surface.^[10a,11,18] The H_2O_2 generated in the SOD-like process can enter the CAT-like dismutation cycle and produce innocuous H_2O and O_2 .^[19] This process makes CeO_2 an excellent antioxidant, which is very detrimental to the realization of the POD-like activity mediated by CeO_2 . Elevating the Ce^{3+} concentration on the surface of CeO_2 considerably contributes to the SOD-like and POD-like activity, which are restrained and transferred to CAT-like activity when the $\text{Ce}^{3+}/\text{Ce}^{4+}$ ratio decreases.^[20] Meanwhile, the CAT-like activity of CeO_2 is highly diminished under an acidic environment, whereas the POD-like activity of CeO_2 is significantly enhanced, accompanied by the SOD activity of CeO_2 slightly affected over a variety of pH changes.^[21] Thus, constructing a CeO_2 -based nanozyme with a high ratio of $\text{Ce}^{3+}/\text{Ce}^{4+}$ and possessing the ability to accelerate the conversion of Ce^{4+} to Ce^{3+} accompanied with the inherent mildly acidic environment in tumor cells is expected to regulate its multi-enzymatic activities elaborately.

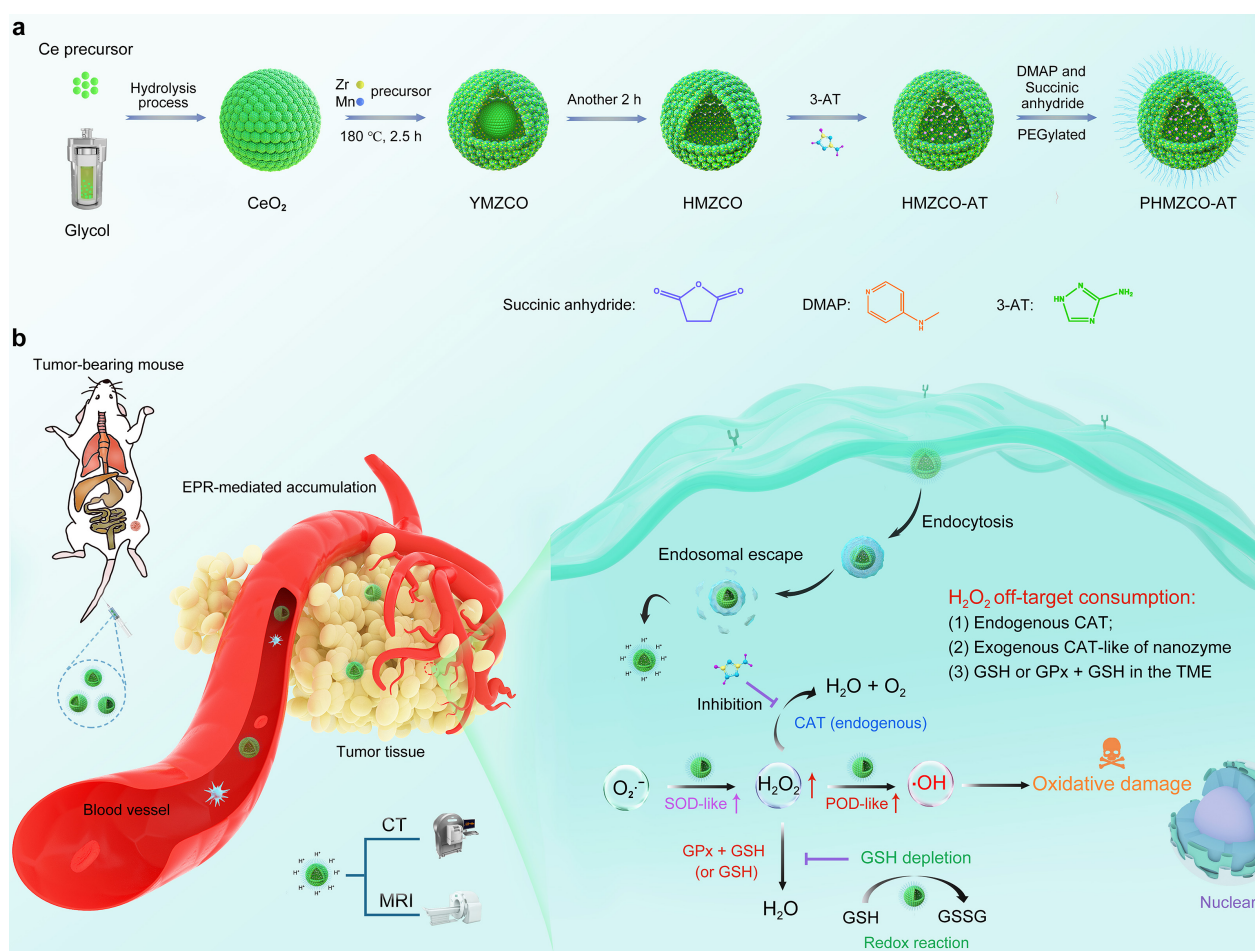


Figure 1. Design, fabrication, and catalysis-based therapeutic schemes of PHMZCO-AT tandem nanozyme. (a) Synthetic procedure of PHMZCO-AT nanozymes with hollow or yolk-shell

structure. (b) Scheme of catalytic H₂O₂ generation, inhibition of the off-target H₂O₂ consumption, and continuous ·OH production for intensive NCDT by PHMZCO-AT nanozymes.

To surmount these limitations, herein, we develop a hollow mesoporous Mn/Zr-co-doped CeO₂ tandem nanozyme (PHMZCO-AT) with elaborately regulated multi-enzymatic activities and function of H₂O₂ homeostasis disruptor. In our work, the controllable formation of hollow Mn/Zr-co-doped CeO₂ (HMZCO) nanozymes is realized by a facile two-step method with the introduction of Zr⁴⁺ and Mn²⁺ *via* the Kirkendall effect. The various morphologies (hollow or yolk-shell) can be easily prepared by only changing the reaction time (**Figure 1a**). Then, the small-molecule 3-amino-1,2,4-triazole (3-AT), an inhibitor of endogenous CAT, is simply deposited into the mesopores or cavities of HMZCO.^[22] The resultant PHMZCO-AT nanozymes with enhanced SOD- and POD-like activity, as well as restrained CAT-like activity compared with pure CeO₂ in a mildly acidic environment, are primarily owing to the acceleration of the redox cycles from Ce⁴⁺ to Ce³⁺ *via* intermetallic charge transfer enabled by the doping of variable-valence Mn ions. In TME, the PHMZCO-AT nanozymes with SOD-like activity are competent to convert the endogenous O₂^{·-} in the tumor region into abundant H₂O₂. The elevated H₂O₂ is then disproportionated by the downstream ones with POD-like activity *via* Fenton-like reactions to produce highly toxic ·OH. Meanwhile, the small 3-AT molecule can be released to inhibit the activity of endogenous CAT to weaken the off-target decomposition of CAT toward H₂O₂. In addition, the consumption of H₂O₂ by GSH with or without GPx can be highly avoided owing to the depletion of GSH by the PHMZCO-AT nanozymes through a redox reaction (Figure S1). *T*₁-weighted magnetic resonance imaging (MRI) and high-contrast X-ray computed tomography (CT) imaging are also realized using the PHMZCO-AT nanozymes on account of the existence of the paramagnetic Mn²⁺ and the high atomic number of elemental Zr, making the therapeutic process visual (**Figure 1b**). In a word, this work provides a proof-of-concept application of Ce-based nanozymes with elaborately regulated multi-enzymatic activities for MRI/CT-guided NCDT by an open-source and reduced off-target H₂O₂ generation strategy.

Results and Discussion

Structure and Composition. The detailed synthetic process of PHMZCO-AT nanozymes is presented in **Figure 1a**. Firstly, monodispersed CeO₂ nanoparticles were synthesized through a hydrolysis process in glycol.^[23] The nanosized crystalline precursors were nucleated to form small particles and then aggregate into larger secondary particles. The secondary particles endow the CeO₂ clusters with high diffusing rates for serving as a suitable template to form various structures

via the Kirkendall effect. As shown in **Figure 2a**, the nanozymes with the yolk-shell (YMZCO) and hollow (HMZCO) morphologies are obtained with the introduction of Zr^{4+} and Mn^{2+} owing to different diffusing rates in this reaction system, in which Zr^{4+} and Mn^{2+} can be readily doped into CeO_2 to form the solid solution. The diffusing rate of the unique secondary CeO_2 nanostructure is much faster than that of the single-crystal nanostructure, simultaneously accompanied by vacancy diffusion. The various morphologies (hollow or yolk-shell) can be simply prepared by only changing the reaction time. Transmission electron microscopic (TEM) image of CeO_2 displays a uniform spherical morphology with a narrow size distribution of approximately 113 nm (**Figure 2b**). The high-resolution TEM (HRTEM) image of CeO_2 shows that the CeO_2 nanosphere is composed of many small nanoparticles and displays an ordered fringe pattern with a lattice spacing of ~ 0.31 nm, which coincides with the (111) facet of CeO_2 face-centered cubic phase (Figure S2a and b). The homogeneous distributions of Ce and O in CeO_2 are revealed by the elemental mapping (Figure S2c). TEM images of the YMZCO and HMZCO nanozymes are displayed in **Figure 2c** and **d**, both of which are highly monodispersed with average diameters of approximately 109.2 and 107.1 nm, respectively (**Figure 2f** and **g**). The yolk-shell and hollow structures are presented clearly by high-angle annular dark-field scanning TEM (HAADF-STEM) and corresponding cross-sectional compositional line profiles. The homogeneous distributions of Ce, O, Zr, and Mn elements in YMZCO and HMZCO nanozymes are revealed by the elemental mapping (**Figure 2i-l**), and the coexistence of Ce, O, Zr, and Mn signals is also displayed from their energy-dispersive spectrometer (EDS) analysis (Figure S3a and b), illustrating the successful synthesis of these nanozymes. Then, the small-molecule 3-AT was loaded into the hollow mesoporous structure of HMZCO nanozymes, yielding HMZCO-AT nanozymes. As shown in **Figure 2e, h, and n**, HMZCO-AT nanozymes show almost the same hollow structure and size distribution (approximately 106.7 nm) to HMZCO. Furthermore, the element mappings present that HMZCO-AT contains Ce, O, Zr, Mn, and N elements (**Figure 2m**), proving the successful and dispersive loading of 3-AT. The EDS spectrum of HMZCO-AT also confirms the presence of Ce, O, Zr, Mn, and N elements as the main components (Figure S3c).

Powder X-ray diffraction (PXRD) patterns indicate that the synthesized CeO_2 and HMZCO can be indexed to face-centered cubic ceria structures (JCPDS no. 34-0394) (**Figure 2p**). No other characteristic peaks assigned to the manganese oxide appears in HMZCO, indicating that Mn^{2+} and Zr^{4+} enter the lattice of CeO_2 to form homogeneous Ce–Zr–Mn–O solid solutions. The diffraction peaks of HMZCO are slightly shifted to higher angles compared with CeO_2 due to the incorporation of smaller-sized Mn^{2+} and Zr^{4+} ions into the ceria lattice giving rise to a decrease in the lattice parameter.^[24] It can be concluded that the YMZCO, HMZCO, and HMZCO-AT nanoparticles are

comprised of numerous small particles with diameters of about 4–5 nm (**Figure 2o**). The inserts in **Figure 2o** are the corresponding selected area electron diffraction (SAED) patterns. The diffraction patterns shown in elongated dots are neither the characteristic polycrystal rings nor the single-crystal dots, suggesting that the big nanoparticles are formed from lots of small nanocrystals oriented in a similar direction. In addition, the doping effect and crystal structure distortion of HMZCO were investigated by Raman spectroscopy with the exciting laser wavelength of 514 nm. As displayed in **Figure 2q**, the main peak at around 460 cm^{-1} corresponds to the F_{2g} stretching mode of the CeO_2 fluorite structure. Compared with pure CeO_2 , the peak location shows a redshift and an increased width of F_{2g} vibrational peak, which could be ascribed to the lattice defects probably due to the substitution of Mn^{2+} and Zr^{4+} in the CeO_2 host lattice. In addition, a weak peak at around 570 cm^{-1} is also observed from the HMZCO nanozymes, attributing to the presence of the oxygen vacancies.^[25]

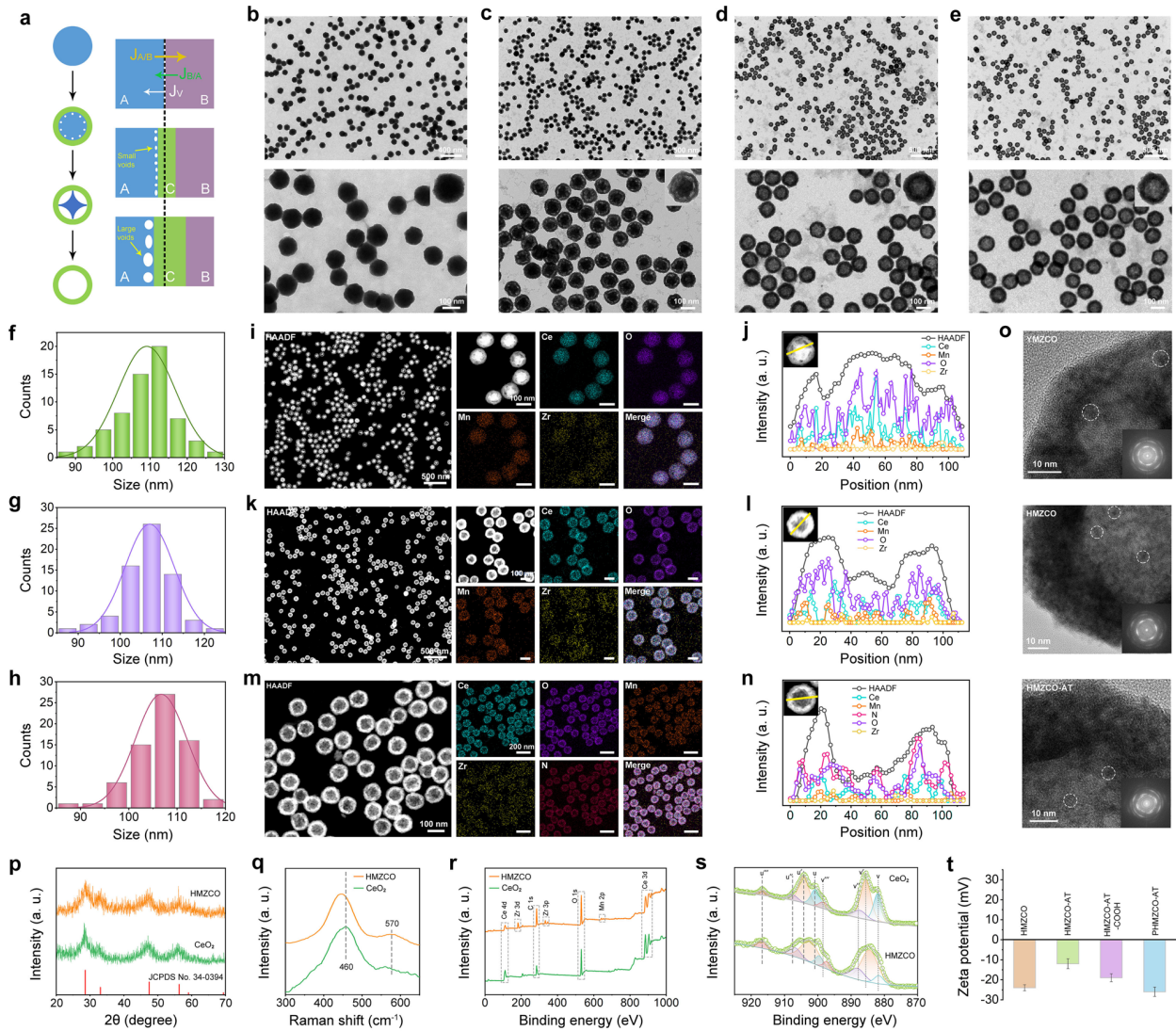


Figure 2. Structural and compositional characterizations. TEM images of (a) CeO_2 , (b) YMZCO, (c) HMZCO, and (d) HMZCO-AT at different magnifications. (e) Illustration about the formation

process of the yolk-shell or hollow structure based on the Kirkendall effect (J_A , J_B , and J_V are diffuse fluxes of CeO_2 clusters, Zr^{4+} and Mn^{2+} , and void, respectively). HAADF-STEM and corresponding elemental mapping of (f) YMZCO, (g) HMZCO, and (h) HMZCO-AT. Cross-sectional compositional line profiles of (i) YMZCO, (j) HMZCO, and (k) HMZCO-AT. Size distributions of (l) YMZCO, (m) HMZCO, and (n) HMZCO-AT. (o) HRTEM images of various nanozymes (inset: corresponding SAED patterns). (p) PXRD patterns, (q) Raman spectra, (r) survey XPS spectra, and (s) high-resolution Ce 3d spectra of CeO_2 and HMZCO. The C 1s binding energy value (284.6 eV) was used as a reference to calibrate the binding energy values of other elements. (t) Zeta potentials of nanozymes at different synthetic steps. Data are presented as mean \pm S.D. ($n = 3$).

X-ray photoelectron spectroscopy (XPS) of the as-synthesized CeO_2 and HMZCO nanozymes was also performed to evaluate the surface chemical compositions (**Figure 2r**). The results show that both nanozymes mainly consist of Ce and O elements, and the coexistence of Mn and Zr signals appear only in the HMZCO nanozymes. High-resolution XPS spectra of Ce element from CeO_2 and HMZCO nanozymes are given in **Figure 2s**, which can be assigned to the spin splitting orbits of $3d_{3/2}$ and $3d_{5/2}$ for the Ce ion (labeled with u and v, respectively). As revealed by previous reports,^[26] the spectra of Ce 3d can be deconvoluted into eight small peaks, marked with v' and u' for Ce^{3+} , v, v'', v''' and u, u'', u''' for Ce^{4+} , thus implying that Ce element is present at the surface of CeO_2 and HMZCO nanozymes in both 4+ and 3+ oxidation states. Meanwhile, the ratio of Ce^{3+} and Ce^{4+} is estimated to be approximately 1.71 for HMZCO and 1.07 for CeO_2 . An increase in the surface $\text{Ce}^{3+}/\text{Ce}^{4+}$ ratio of the HMZCO nanozymes can promote the SOD- and POD-like activities, as well as restrain the CAT-like activity. It is worth noting that the spilled peaks of HMZCO exist at lower binding energies compared with CeO_2 , presumably because that the chemical environment of the surface Ce ions is affected by the variable-valence Mn^{2+} dopants.^[24,27] In general, the shifting of binding energy toward lower side can be ascribed to electron reception, implying that the conversion of Ce^{4+} to Ce^{3+} can be accelerated through the doping of variable-valence metal ions.^[28] In addition, the XPS spectrum of Mn 2p displays two peaks at 653.5 and 641.8 eV, which can be attributed to Mn $2p_{1/2}$ and Mn $2p_{3/2}$ states, respectively (Figure S4). Accordingly, the observed binding energy suggests that Mn is in +2 and +3 oxidation states.^[24] Thus, it is clear that the electrons migrate partially from the Mn site to the Ce site, accompanied by the reduction of a part of Ce^{4+} to Ce^{3+} in the surface region with the redox equilibrium $\text{Ce}^{4+} + \text{Mn}^{2+} \leftrightarrow \text{Ce}^{3+} + \text{Mn}^{3+}$. The Mn content in the HMZCO nanozymes is determined to be 5.2 wt%, estimated by XPS quantitative analysis.

N₂ adsorption/desorption measurements were used to investigate the textural characters of the as-synthesized HMZCO and HMZCO-AT nanozymes. As shown in Figure S5, the specific surface area of the HMZCO nanozymes analyzed by the Brunauer–Emmett–Teller method is determined to be 194.34 m² g⁻¹, and the primary pore size distribution is in the range of 4–10 nm with a minor peak at 4.5 nm (average pore size: 9.1 nm). The HMZCO-AT nanozymes show a decreased surface area of 108.34 m² g⁻¹ and a mean pore size of 5.3 nm compared to HMZCO, indicating the successful encapsulation of 3-AT. Meanwhile, relatively large surface area and pore size of both HMZCO and HMZCO-AT nanozymes can provide more adsorption or reaction active sites and improved accessibility for various substrates (O₂^{·-} or H₂O₂), which are favorable for achieving high catalytic performance. In addition, thermogravimetric analysis was conducted to evaluate the loading amount of 3-AT in the HMZCO-AT nanozymes (Figure S6), which is 7.02%. To endow the HMZCO-AT nanozymes with higher biocompatibility, NH₂-PEG-COOH (*M_w* = 4000) was employed for surface functionality *via* amide formation. The stepwise altered zeta potentials in different systems from -24 mV to -12, -19, and -36 mV indicate the successful loading of 3-AT and surface functionalization (**Figure 2t**). To analyze the stability of PHMZCO-AT nanozymes, dynamic light scattering measurements were carried out to monitor the average size and corresponding polydispersity index (PDI) of PHMZCO-AT in RPMI 1640 medium +10% FBS at various pH (pH 7.4 and pH 6.0) and phosphate-buffered saline (PBS) within 7 days (Figure S7). It can be observed that PHMZCO-AT nanozymes show a uniform hydrated particle size and display no apparent PDI change in different solutions within 7 days, which suggest that the nanozymes possess excellent stability for ensuring their continuous catalysis in the physiological environment, especially in the TME.

***In Vitro* Evaluation of the SOD-like and CAT-like Activity and GSH Depletion of PHMZCO-AT Nanozymes.** Because O₂^{·-} is perpetually generated in body metabolism, especially in the tumor cells with abnormal metabolism, SOD, as a vital enzyme in various cells, catalyzes the dismutation of O₂^{·-} into H₂O₂. Thus, SOD mimetics are competent to serve as an H₂O₂ producer in TME.^[29] We initially assessed the SOD-like activity of PHMZCO-AT nanozymes through the typical nitroblue tetrazolium (NBT) chromogenic assay, in which O₂^{·-} was generated by L-methionine and riboflavin upon the irradiation of UV, reducing NBT to formazan with a characteristic peak at 560 nm (**Figure 3a**). It is noteworthy that the absorbance intensity declines with increasing PHMZCO-AT concentration, indicating that PHMZCO-AT nanozymes are gifted with effective SOD-like activity (**Figure 3b**). As shown in **Figure 3c**, the inhibition percentage of PHMZCO-AT is higher than pure CeO₂ under the same experimental conditions, demonstrating the enhanced SOD-like

activity of PHMZCO-AT nanozymes due to the high ratio of $\text{Ce}^{3+}/\text{Ce}^{4+}$ and accelerated conversion from Ce^{4+} to Ce^{3+} . Considering that the nanozyme-based catalytic activities are highly dependent on the pH value, we further analyzed the influence of the pH on the SOD-like activity. The result shows that the SOD-like activity of PHMZCO-AT presents a certain improvement in the mildly acidic environment (Figure S8). In addition, the SOD-like activity of PHMZCO-AT nanozymes can also be testified by detecting the nanozyme-triggered H_2O_2 generation by employing xanthine as the $\text{O}_2^{\cdot-}$ generator in the presence of xanthine oxidase (XOD) and Amplex red as the probe, where Amplex red can react with H_2O_2 to produce a red Resorufin with a typical absorption peak at 571 nm (**Figure 3d**). As expected, there is a distinct increase in the Resorufin absorption intensity as a function of the nanozyme concentration, and the produced H_2O_2 content can be calculated by the standard curve of Resorufin *versus* H_2O_2 concentrations (**Figure 3e**), suggesting that PHMZCO-AT nanozymes possess the SOD-like activity to produce H_2O_2 (**Figure 3f**). For comparison, the amount of generated H_2O_2 catalyzed by CeO_2 was testified with identical treatment, showing the enhanced SOD-like catalytic activity of PHMZCO-AT nanozymes as compared with pure CeO_2 (**Figure 3g**). The result is consistent with the above NBT chromogenic measurement.

As the primary endogenous antioxidant, GSH plays an irreplaceable role in keeping the redox balance of biological systems. It is well known that the high concentration of GSH in the tumor (approximately 1000-folds higher than normal tissues) can deplete the generated H_2O_2 with or without the assistance of GPx in TME, thus resulting in the off-target expenditure of H_2O_2 . Hence, GSH depletion may be a facile and effective approach to achieve the H_2O_2 accumulation for intensive NCDT. The GSH depletion capacity of PHMZCO-AT nanozymes was evaluated based on a GSH indicator, i.e., 5,5'-dithiobis-(2-nitrobenzoic acid) (DTNB), which could be reduced by GSH to generate the yellow products with the characteristic absorbance at 412 nm (**Figure 3h and i**). In the presence of PHMZCO-AT nanozymes, the GSH concentration can be observed at different time points, and the GSH content gradually decreased upon the incubation time (**Figure 3j and k**). XPS analysis shows that the ratio of $\text{Ce}^{3+}/\text{Ce}^{4+}$ increases from an initial 1.71 to 2.3 after the reaction with GSH, suggesting that a part of Ce^{4+} on the surface was reduced to Ce^{3+} by GSH (Figure S9). The consumption of GSH by PHMZCO-AT nanozymes is favorable for retaining a relatively high content of H_2O_2 in tumor cells in the process of NCDT.

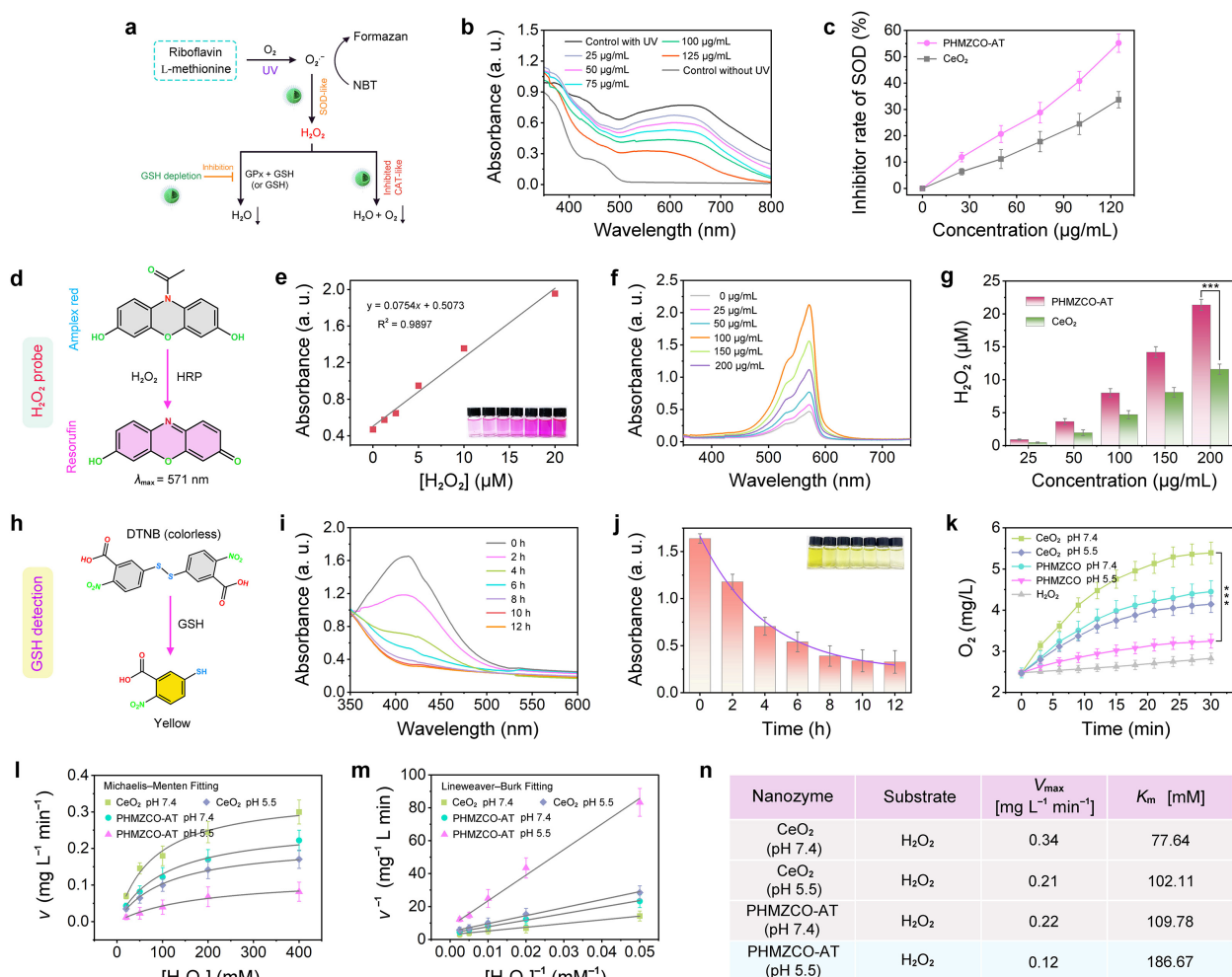


Figure 3. *In vitro* evaluations of the SOD-like and CAT-like catalytic activity and GSH depletion of PHMZCO-AT nanozymes. (a) Schematic representation of the H_2O_2 generation and inhibition of the off-target H_2O_2 consumption enabled by the PHMZCO-AT nanozymes. (b) Catalytic conversion of $\text{O}_2^{\cdot-}$ by different concentrations of PHMZCO-AT nanozymes. (c) SOD-like activity of PHMZCO-AT nanozymes. (d) Reaction of Amplex red with H_2O_2 to form the red Resorufin products (H_2O_2 detection). (e) Standard curve of Resorufin *versus* H_2O_2 concentrations detected at 571 nm. (f) H_2O_2 generation catalyzed by PHMZCO-AT nanozymes using Amplex red as a probe. (g) Comparison of H_2O_2 production in the presence of CeO_2 or PHMZCO-AT nanozymes. Data are defined as mean \pm S.D. ($n = 3$). Statistical significance is assessed by unpaired Student's two-sided t -test, *** $p < 0.001$. (h) Reaction of colorless DTNB with GSH to form the yellow products (GSH detection). (i, j) Time-dependent GSH consumption with PHMZCO-AT nanozymes. The inset in (j) is a photograph of the solutions at different reaction times. Data are defined as mean \pm S.D. ($n = 3$). (k) O_2 generation with different treatments. Statistical significance is assessed by unpaired Student's two-sided t -test, *** $p < 0.001$. (l) Michaelis-Menten kinetic analysis and (m) Lineweaver-Burk plotting of CAT-like activity with H_2O_2 as a substrate. (n) Comparison of the

kinetic parameters of CAT-like activity. Data are presented as mean \pm S.D., and error bars shown represent the standard error derived from three independent measurements.

Nanozymes with CAT-like activity have a well-known ability to catalyze the decomposition of H_2O_2 to H_2O and O_2 , thereby achieving H_2O_2 off-target consumption to inhibit H_2O_2 accumulation. Considering this process, the CAT-like activity of PHMZCO-AT nanozymes can be largely inhibited through tuning the ratio of $\text{Ce}^{3+}/\text{Ce}^{4+}$ and accelerating the conversion from Ce^{4+} to Ce^{3+} , as well as utilizing the pH of the reaction environment (Figure S10).^[17a] These assumptions were proven in the following experiments. Initially, the O_2 generation amounts in the presence of CeO_2 or PHMZCO-AT nanozymes at pH 7.4 and 5.5 were detected with dissolved oxygen meter, in which the O_2 generation content of PHMZCO-AT nanozymes at pH 5.5 largely decreased when compared with pure CeO_2 at pH 7.4 and 5.5 (**Figure 3k**). To reveal the CAT-like enzymatic catalysis mechanism, a steady-state kinetic analysis was performed by changing the concentration of H_2O_2 (20, 50, 100, 200, and 400 mM) at a fixed concentration of CeO_2 or PHMZCO-AT, which was consistent with the classic Michaelis–Menten kinetics (**Figure 3l**). According to the corresponding Lineweaver–Burk plots (**Figure 3m**), the enzyme kinetic parameters, including maximum reaction velocity (v) and Michaelis–Menten constants (K_m) were calculated, in which K_m confirms the affinity of the nanozyme to the substrate (low K_m indicates a high affinity) and V_{\max} represents the catalytic activity of the nanozyme (**Figure 3n**).^[30] The values of K_m and V_{\max} were solved to be 77.64 mM and $0.34 \text{ mg L}^{-1} \text{ min}^{-1}$ for the pure CeO_2 nanozymes at pH 7.4, while those of PHMZCO-AT nanozymes at pH 5.5 were 180.67 mM and $0.12 \text{ mg L}^{-1} \text{ min}^{-1}$ according to the following equations, respectively.

The elevated K_m and reduced V_{\max} indicate significantly decreased catalytic capability of PHMZCO-AT nanozymes at pH 5.5 (Equations (1) and (2)). These results demonstrate that CAT-like activity of PHMZCO-AT nanozymes can be highly inhibited under a tumorous acidic pH environment and thus reduce the off-target consumption of H_2O_2 to a large extent with the assistant of GSH depletion.

$$v_0 = \frac{V_{\max} [S]}{K_m + [S]} \quad (1)$$

$$\frac{1}{v_0} = \frac{K_m}{V_{\max}} \cdot \frac{1}{[S]} + \frac{1}{V_{\max}} \quad (2)$$

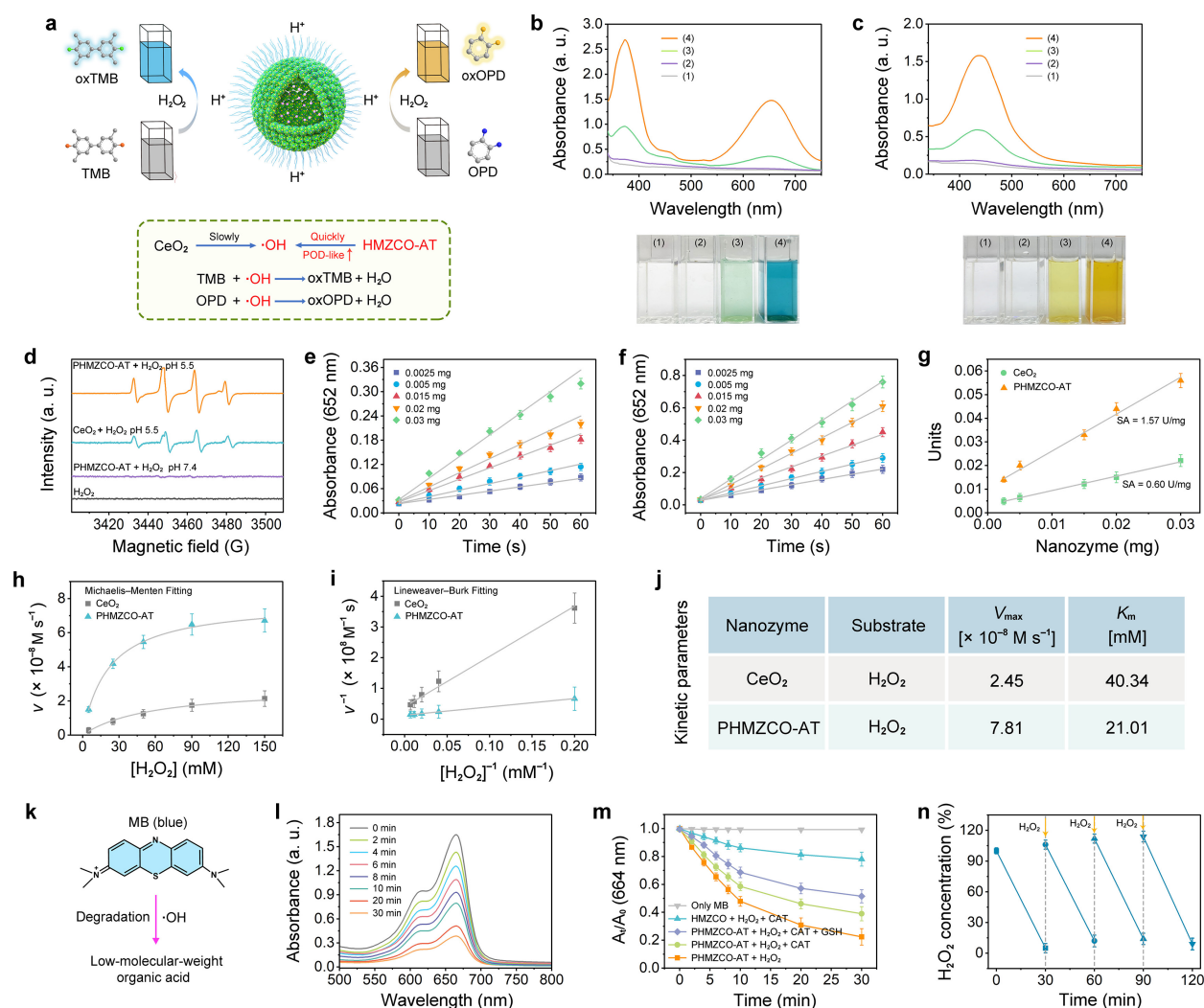


Figure 4. *In vitro* assessments of the POD-like catalytic activity for PHMZCO-AT nanozymes. (a) Schematic illustration of the POD-like catalytic process of PHMZCO-AT nanozymes. UV-vis absorption spectra (upper panel) of the catalyzed oxidation for (b) TMB (oxTMB) and (c) OPD (oxOPD) as catalyzed by: (1) control, (2) H_2O_2 , (3) $\text{CeO}_2 + \text{H}_2\text{O}_2$, and (4) PHMZCO-AT + H_2O_2 in the reaction buffer (pH 5.5). The bottom panel presents corresponding digital photographs of each group. (d) ESR spectra of $\cdot\text{OH}$ trapped by DMPO under different conditions. Initial linear portion of reaction-time curves for (e) CeO_2 and (f) PHMZCO-AT nanozymes. (g) Specific activities of CeO_2 and PHMZCO-AT nanozymes. (h) Michaelis-Menten curves and (i) Lineweaver-Burk plotting of CeO_2 and PHMZCO-AT nanozymes. (j) Comparison of the kinetic parameters for POD-like activity. (k) Reaction of MB with $\cdot\text{OH}$ to form the colorless products. (l) Degradation of MB by the PHMZCO-AT-mediated Fenton-like reaction at different time points. (m) Influence of CAT and GSH on the MB degradation by the PHMZCO-AT-catalyzed Fenton-like reaction. (n) Repetitive catalytic ability of PHMZCO-AT nanozymes with repetitive addition.

of H_2O_2 . Error bars shown represent the standard error obtained from three independent experiments. Data are defined as mean \pm S.D. ($n = 3$).

***In vitro* Assessments of POD-Like Activity of PHMZCO-AT Nanozymes.** Encouraged by the unique electronic structure of PHMZCO-AT nanozymes with the doping of variable-valence Mn^{2+} , in which the Mn dopants can serve as electron reservoir and promote the electron transfer between Ce and H_2O_2 ,^[27] we speculated that the PHMZCO-AT can act as an effective POD-like nanozyme to catalyze H_2O_2 into $\cdot\text{OH}$ through the classic Fenton-like reaction. Firstly, representative colorimetric assays employing 3,3',5,5'-tetramethyl-benzidine (TMB) and o-phenylenediamine (OPD) were utilized to validate the POD-like activity of PHMZCO-AT nanozymes. In the presence of H_2O_2 , PHMZCO-AT nanozymes can catalyze the oxidation of TMB to generate blue oxTMB with the characteristic absorbance at 370 and 652 nm, and oxidize OPD to form yellow-colored oxOPD with a typical peak at 417 nm in PBS with the pH value of 5.5 (**Figure 4a**). As illustrated in **Figure 4b** and **c**, the absorbance intensity of the group treated with PHMZCO-AT + H_2O_2 shows an apparent increase compared with that incubated with H_2O_2 or $\text{CeO}_2 + \text{H}_2\text{O}_2$, indicating the enhanced POD-like activity of PHMZCO-AT nanozymes. The enhanced activity can be intuitively observed from the digital photographs. Meanwhile, the generation of $\cdot\text{OH}$ was evaluated through the electron spin resonance (ESR) spectra using 5,5-dimethyl-1-pyrroline-N-oxide (DMPO) as the $\cdot\text{OH}$ trapping agent. The characteristic peak intensity of PHMZCO-AT at pH 5.5 in the presence of H_2O_2 shows much stronger intensity than that in the H_2O_2 only, PHMZCO-AT + H_2O_2 (pH 7.4), and $\text{CeO}_2 + \text{H}_2\text{O}_2$ (pH 5.5) groups (**Figure 4d**), confirming that PHMZCO-AT nanozymes possess the pH-dependent catalytical activity and excellent POD-like activity.

To further assess the POD-like catalytic activity of PHMZCO-AT nanozymes, the specific activity values (U mg^{-1}) were quantitatively evaluated by measuring the absorption intensity of the PHMZCO-AT-driven colorimetric reactions.^[31] The slopes of the initial linear part of the reaction curve for CeO_2 and PHMZCO-AT nanozymes at different concentrations were calculated and then plotted with the corresponding mass to determine the specific activity value (**Figure 4e** and **f**). As shown in **Figure 4g**, the PHMZCO-AT nanozymes (1.57 U mg^{-1}) show much higher catalytic activity compared to pure CeO_2 (0.60 U mg^{-1}). We further investigated the catalytic mechanism and determined the kinetic parameters of PHMZCO-AT nanozymes, which coincided with the Michaelis–Menten model (**Figure 4h**). The K_m and V_{\max} were calculated from Lineweaver–Burk plots (**Figure 4i**). The relevant kinetic parameters are listed in **Figure 4j**, in which the declined K_m value and elevated V_{\max} values of PHMZCO-AT nanozymes imply the enhanced POD-like catalytic activity. In addition, the PHMZCO-AT nanozymes perform higher POD-like catalytic

activity than most of the reported nanozymes as estimated from the values of V_{\max} and K_m (Table S1).

A methylene blue (MB) decoloration experiment was also employed to demonstrate the production of $\cdot\text{OH}$ by the PHMZCO-AT nanozymes in the presence of H_2O_2 (**Figure 4k**). As displayed in **Figure 4l**, the absorbance of MB gradually decreases upon prolonging the reaction time, suggesting the production of $\cdot\text{OH}$ catalyzed by the PHMZCO-AT nanozymes. In addition, the off-target depletion of H_2O_2 by CAT and GSH is responsible for the unsatisfactory NCDT performance. Considering that the enzymatic activity of CAT can be retarded by the loaded 3-AT molecule by covalently binding to its active center, we assessed the degradation of MB by PHMZCO-AT in the presence of H_2O_2 and natural CAT. It can be found that the PHMZCO-AT nanozymes show an elevated degradation ratio of MB compared with HMZCO plus H_2O_2 in the presence of natural CAT, attributing to the inhibition effect of 3-AT on the catalytic activity of CAT (**Figure 4m**). More importantly, owing to the consumption of GSH and restrained CAT activity by PHMZCO-AT nanozymes, PHMZCO-AT nanozymes can degrade about 49% MB even at a high GSH concentration of 6 mM, confirming that PHMZCO-AT nanozymes can greatly reduce the off-target depletion of H_2O_2 by GSH and CAT and boost the production of $\cdot\text{OH}$ catalyzed by the PHMZCO-AT-mediated Fenton-like reaction. Furthermore, the PHMZCO-AT nanozymes could persistently catalyze H_2O_2 even after several cycles of H_2O_2 addition, confirming that PHMZCO-AT nanozymes possess sustained catalytic activity (**Figure 4n**). These results collectively indicate that the PHMZCO-AT nanozymes could function as a tumor-specific theranostic agent with enhanced and long-circulating POD-like activity to achieve effective and steady NCDT.

Density Functional Theory Calculations. To vividly elucidate the catalysis mechanism that how Mn and Zr atoms affect the SOD and POD activity of PHMZCO-AT nanozymes through accelerating the conversion of Ce^{4+} to Ce^{3+} accompanied by the generation of oxygen vacancy, the first-principles calculations within density functional theory (DFT) were implemented by the Vienna ab-initio Simulation Package.^[32] We built several models of ideal CeO_2 (110) surface, Mn-doped CeO_2 (110) surface, Mn-doped (110) CeO_2 surface with O defect, and Zr-doped CeO_2 (110) surface to explore the SOD- and POD-like catalytic process (Figure S11). Considering that the surface adsorption and activation of reactants by nanozymes are both critical steps in heterogeneous catalysis, the interaction between reactants and various surfaces was then evaluated from these two aspects without considering the desorption of products. As shown in Table S2, due to the introduction of Mn and Zr dopants, the bonding properties of CeO_2 are changed, and the oxygen

vacancy (Ov) formation energy (ΔE_{Ov}) is reduced from 3.75 eV to 2.94 eV for Zr-CeO₂ and 2.30 eV for Mn-CeO₂, indicating that Mn dopant facilitates the formation of Ov within the local environment of CeO₂ crystal. Meanwhile, the electron density around the Ce atom of the Mn-CeO₂ surface is higher than that of CeO₂ and Zr-CeO₂ accompanied by the decreased Bader charges (Figure S12), indicating that Mn substitution plays a critical role to boost the structure reconstruction and subsequently induce the reduction of Ce⁴⁺ to Ce³⁺. Furthermore, to evaluate how the change of surface environments affects the activation process, relevant reaction barriers were calculated based on the Nudged Elastic Band method. $\cdot O_2^-$ is a Brønsted base, which is readily converted to HO₂ \cdot in water *via* the reversible reaction (Equation (3)):[33]



To study its SOD-mimetic mechanisms, the two HO₂ \cdot radicals are added to the different surfaces, in which the chemisorption of two HO₂ \cdot radicals would react with each other and lead to the generation of surface O₂* and H₂O₂*. The detailed mechanism and the energy profiles of the reactions are shown in Figure S13, which are exoenergetic with energy change (ΔE) of -2.42, -3.54, -4.0, and -2.49 eV for ideal CeO₂ (110) surface, Mn-doped CeO₂ (110) surface, Mn-doped (110) CeO₂ surface with O defect, and Zr-doped CeO₂ (110) surface, respectively. This result suggests that the disproportionation of HO₂ \cdot into O₂* and H₂O₂* by the various surfaces is thermodynamically favorable, especially for the Mn-doped surface. Notably, the activation energy barrier (E_a) for the rate-determining step of Mn-doped CeO₂ (110) surface and Mn-doped (110) CeO₂ surface with O defect is 0.12 and 0.27 eV respectively, suggesting higher SOD-like activity after the incorporation of Mn atom.

The POD-like catalytic process involving the adsorption of H₂O₂ and subsequential O–O bond cleavage with the generation of a surface OH group and a $\cdot OH$ radical was evaluated on various surfaces.[34] Figure S14 shows the critical intermediate structures along the reaction path and the energy profiles during the H₂O₂-decomposition process. The calculated energy profiles indicate that the cleavage of O–O bond in the activation process is the rate-determining step, in which the Mn-doped (110) CeO₂ surface with O defect shows the lowest energy barrier (E_a = 0.62 eV) as compared with the pristine CeO₂ (110) surface (E_a = 1.81 eV), Mn-doped CeO₂ (110) surface (E_a = 1.38 eV), and Zr-doped CeO₂ (110) surface (E_a = 1.50 eV), indicating that H₂O₂ molecule is easily adsorbed and dissociated on the O_v active site. These results, combined with the experimental evaluation about the effect of Zr doping on the enzyme-like activity, suggest that the enhanced SOD-and POD-like activity of PHMZCO-AT nanozymes is mainly caused by Mn substitution-induced local structure reconstruction along with the Ov generation and the electron transfer from Mn to the surrounding Ce atom to enhance the numbers of reductive Ce³⁺ (Figure

S15). This conclusion is verified by the electron density distribution of different surfaces and is in line with our experimental results. Meanwhile, the schematic illustration for the leading enzymatic activity of PHMZCO-AT nanozymes in different environments is given in Figure S16.

***In Vitro* NCDT Evaluations.** Inspired by the excellent catalytic performance of PHMZCO-AT nanozymes with elaborately regulated multi-enzymatic activities, the *in vitro* therapeutic efficacy was evaluated against murine 4T1 breast cancer cells. At the beginning, the subcellular localization of fluorescein isothiocyanate (FITC)-labeled PHMZCO-AT nanozymes was studied by flow cytometry and confocal laser scanning microscopy (CLSM). The flow cytometry result shows the nanozymes can be endocytosed easily by 4T1 cells in a time-dependent manner (Figure S17 and S18). Furthermore, we utilized LysoTracker Red, a lysosome binding probe, to acquaint the cellular phagocytosis mechanism of the nanozymes. As shown in **Figure 5a-c**, the Pearson's coefficient (PC) representing the colocalization between FITC fluorescence of FITC-labeled PHMZCO-AT nanozymes and LysoTracker is determined to be 0.7737 at 1.5 h post-incubation through the Image J analysis, indicating that PHMZCO-AT nanozymes are internalized by the 4T1 cells *via* the endolysosomal pathway. After incubation for 3 h, the fluorescence of nanozymes increases and gradually separates from the red signals of LysoTracker with the PC of 0.4958, indicating the efficient endosomal escape of PHMZCO-AT nanozymes after cellular uptake possibly due to the classic "proton sponge" effect.^[35] This process is a critical prerequisite for achieving the curative effect of the as-constructed nanozymes. Furthermore, bio-TEM images exhibit that the hollow PHMZCO-AT nanozymes could be observed in the lysosome and cytoplasm after incubation with 4T1 cells for 2 h (**Figure 5d and e**), which well match with the colocalization experiment.

Highly expressed $O_2^{\cdot-}$ in tumor cells is an essential prerequisite for promoting H_2O_2 evolution by PHMZCO-AT nanozymes. It is well-known that $O_2^{\cdot-}$ is the parent ROS produced in the cellular environment, especially in the tumor cells with abnormal metabolism. Therefore, the content of $\cdot O_2^-$ in PHMZCO-AT-treated cells at different time intervals was observed by employing the dihydroethidium probe, which could emit red fluorescence in the presence of $\cdot O_2^-$.^[36] As shown in Figure S19, the fluorescence intensity gradually decreases with the extension of incubation time, suggesting the effective consumption of $\cdot O_2^-$ in the presence of PHMZCO-AT nanozymes. We further investigated the intracellular generation of H_2O_2 by using Amplex red as an H_2O_2 probe.^[37] As displayed in Figure S20, the strongest red fluorescence was observed at 0.5 h post-incubation, owing to the conversion of $\cdot O_2^-$ into H_2O_2 by the SOD-like activity of PHMZCO-AT. Moreover, the declined fluorescence intensity after the incubation for 2 h confirmed the decreased content of H_2O_2 , which should be ascribed to the subsequent consumption by

PHMZCO-AT nanozymes to produce $\cdot\text{OH}$. Next, the CAT-like activity of PHMZCO-AT nanozymes in 4T1 cells was investigated with $[\text{Ru}(\text{dpp})_3]^{2+}\text{Cl}_2$ as an oxygen probe, the red fluorescence of which can be quenched by O_2 . As shown in **Figure 5f**, the group treated with nanozymes displays the highest fluorescence compared to other groups (control, CeO_2 , and HMZCO). Semiquantification of the mean fluorescence intensity through ImageJ software displays that the group treated with PHMZCO-AT nanozymes is approximately 3.4-times higher than that of the CeO_2 group, and 1.2-folds higher than the control group (Figure S21), indicating the restraint of endogenous CAT activity by PHMZCO-AT nanozymes. In addition, the GSH consumption by PHMZCO-AT nanozymes at a cellular level was evaluated by using the commercial intracellular GSH probe of Thiol Tracker violet on 4T1 cells. As observed in the CLSM images shown in **Figure 5g**, the PHMZCO-AT-treated cells present weaker green fluorescence, and the intensity declines upon increasing the concentration, demonstrating that the intracellular GSH content decreases notably. These results indicate that the off-target depletion of H_2O_2 can be highly restrained due to the GSH depletion, the suppression of endogenous CAT activity, and exogenous CAT-like activity by PHMZCO-AT.

To evaluate intracellular ROS-generated capacity of PHMZCO-AT nanozymes, fluorescence microscopy assays by using 2',7'-dichlorofluorescein diacetate (DCFH-DA) probe were conducted. The 4T1 cells incubated with PHMZCO-AT nanozymes exhibit higher green fluorescence compared with other groups (**Figure 5h**), confirming the massive intracellular ROS. The flow cytometry analysis was employed to semiquantitatively examine the efficiency of ROS generation (**Figure 5i**), in which the group treated with PHMZCO-AT nanozymes presents the highest mean fluorescence intensity (**Figure 5j**). Both CLSM and flow cytometry results confirm that the intracellular ROS generation catalyzed by PHMZCO-AT nanozymes is substantially promoted owing to the high accumulation of H_2O_2 in 4T1 cells. To specifically detect the generation of $\cdot\text{OH}$, the $\cdot\text{OH}$ probe aminophenyl fluorescein was then employed to study the intracellular CDT process.^[38] The amount of $\cdot\text{OH}$ in 4T1 cells exhibits time-dependent augmentation, indicating the superior POD-like catalytic activity (Figure S22). The cytocompatibility of PHMZCO-AT nanozymes to L929 fibroblast cells (a normal cell line) and the *in vitro* cytotoxicity profiles toward 4T1 cells were investigated using standard methyl thiazolyl tetrazolium (MTT) assay. The PHMZCO-AT nanozymes present slight effects on the proliferation of the L929 fibroblast cells at the elevated concentration up to $200\text{ }\mu\text{g mL}^{-1}$ within 12 and 24 h (Figure S23). In the 4T1 cytotoxicity assay, all therapeutic groups display concentration-dependent cytotoxicity. The viability of 4T1 cells treated with PHMZCO-AT nanozymes significantly decreases, showing a high inhibition rate (70%) at $200\text{ }\mu\text{g mL}^{-1}$ after 24 h incubation (**Figure 5k**). These results confirm

that the PHMZCO-AT nanozymes can trigger the generation of abundant and highly toxic $\cdot\text{OH}$ to result in the apoptosis of 4T1 cells with high specificity, while avoiding the undesired side effect to normal cells.

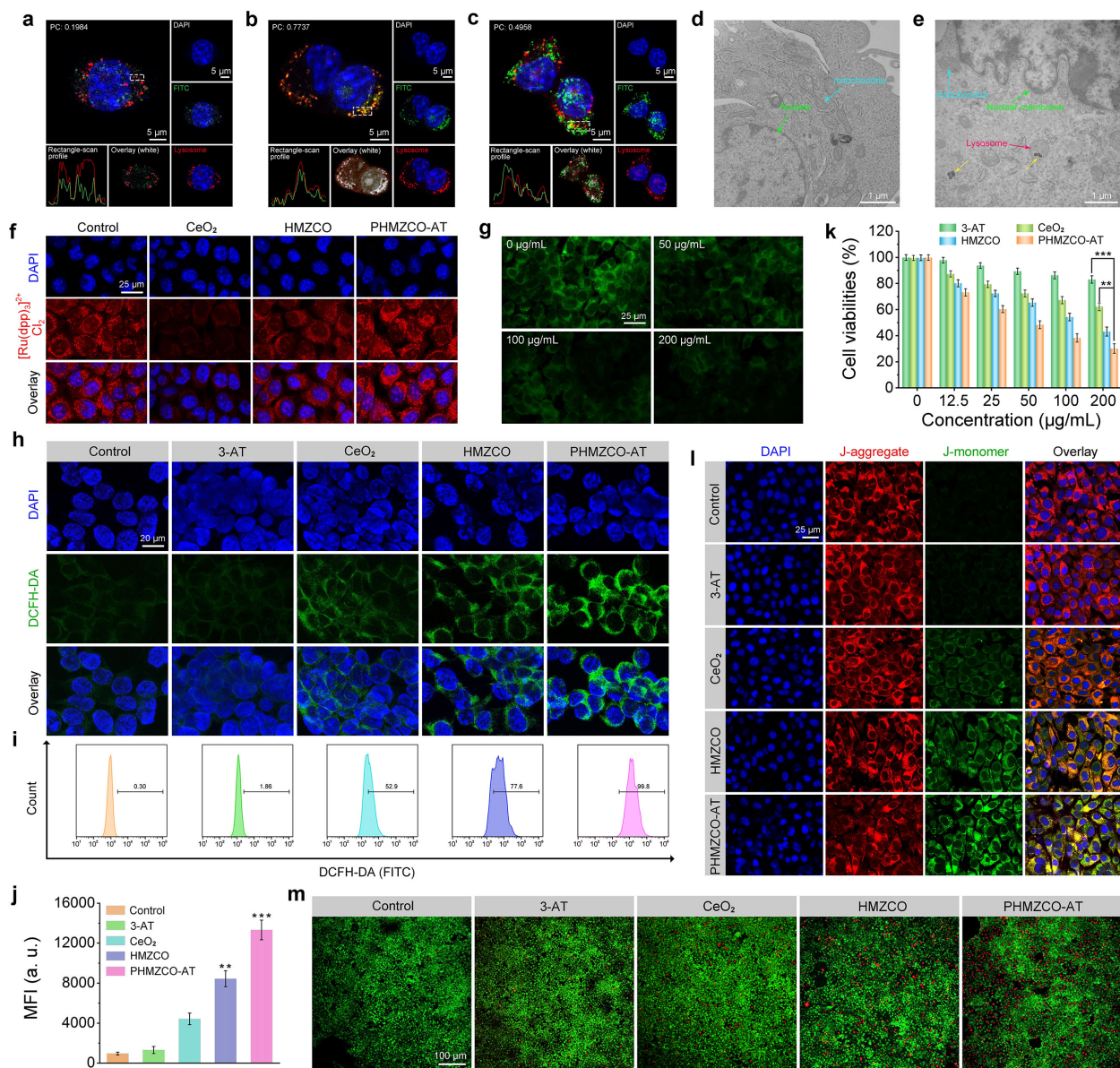


Figure 5. Cellular uptake and *in vitro* NCDT evaluation for PHMZCO-AT nanozymes. (a–c) Co-localization between FITC-labeled PHMZCO-AT nanozymes and lysosome in 4T1 cells under CLSM at different time intervals (0.5, 1.5, and 3 h). Representative bio-TEM images of 4T1 cells incubated with PHMZCO-AT nanozymes for (d) 0 h and (e) 2 h (yellow arrows indicate the internalized nanozymes). (f) Intracellular O_2 generation using $[\text{Ru}(\text{dpp})_3]^{2+}\text{Cl}_2$ as a probe incubated with different samples for 2 h. (g) CLSM images of 4T1 cells treated with PHMZCO-AT nanozymes (0–200 $\mu\text{g}/\text{mL}$) and then stained with an intracellular GSH probe, i.e., thiol Tracker Violet. (h) CLSM images, (i) flow cytometry analysis, and (j) corresponding mean fluorescence intensity of intracellular ROS level with different treatments. Data are presented as mean \pm S.D. (n

= 3). Statistical significance is evaluated by unpaired Student's two-sided t test, i.e., $**P < 0.005$, $***P < 0.001$ for PHMZCO-AT and HMZCO groups compared with the control group. (k) Cytotoxicity profiles, (l) JC-1 staining, and (m) Calcein-AM/PI double staining of 4T1 cells in different groups: control, 3-AT, CeO₂, HMZCO, and PHMZCO-AT. Data are presented as mean \pm S.D. (n = 3). Statistical significance is analyzed by unpaired Student's two-sided t test, $**P < 0.005$, $***P < 0.001$.

Moreover, the mitochondrial integrity was examined through JC-1 staining, since the cell apoptosis is highly related to the dysfunction of mitochondria. As seen from **Figure 5l**, the group treated with PHMZCO-AT exhibits the highest fluorescence ratio of green monomer to red aggregate, indicating that abundant mitochondria are damaged. Then, the representative flow cytometric apoptosis assay after stained with Annexin V-FITC and propidium iodide (PI) was conducted to reveal the antitumor mechanism of $\cdot\text{OH}$ -mediated NCDT. The apoptotic ratio induced by PHMZCO-AT nanozymes, i.e., 58.2% (sum of Q2 + Q3), is significantly higher than that of 3-AT (5.16%), CeO₂ (24.58%), and HMZCO (43.7%) under the same condition, demonstrating that PHMZCO-AT-mediated cell toxicity is associated with early apoptosis and late apoptosis (Figure S24). In addition, the anticancer performance was further testified through the calcein-AM and PI double-staining assay (**Figure 5m**). These *in vitro* results demonstrate the efficient NCDT as contributed by the PHMZCO-AT-enabled H₂O₂ accumulation and subsequently catalytic generation of highly toxic $\cdot\text{OH}$ *via* cascade catalytic reactions.

In Vitro and in Vivo MRI and CT Imaging. Considering that paramagnetic Mn²⁺ species is a T_1 -shortening agent,^[39] we envisaged that PHMZCO-AT nanozymes can achieve contrast-enhanced T_1 -MRI (**Figure 6a**). The *in vitro* T_1 -weighted MRI performance of PHMZCO-AT nanozymes after being incubated in PBS at different pH (5.5, 6.5, and 7.4) for 7 h was investigated. As shown in **Figure 6b**, the remarkable concentration-dependent brightening effect of PHMZCO-AT nanozymes was observed in T_1 -MR images at pH 5.5, whereas the signals of nanozymes in pH 6.5 and 7.4 PBS appeared to be much weaker. Importantly, the longitudinal relaxation rate (r_1) is significantly enhanced from the initial value of 0.30 mM⁻¹ s⁻¹ at pH 7.4 to 0.65 mM⁻¹ s⁻¹ and 1.41 mM⁻¹ s⁻¹ after incubation in pH 6.5 and 5.5 PBS for 7 h respectively, attributing to the boosted Mn²⁺ ion release under acidic conditions and enhanced accessibility with the surrounding water molecule (**Figure 6c**). This phenomenon demonstrates that PHMZCO-AT nanozymes with pH-responsive T_1 -MR contrasting performance have a promising potential for tumor-specific imaging. Thus, the MRI performance was verified in 4T1 tumor-bearing mice after intravenous (i.v.)

injection of PHMZCO-AT nanozymes at the given time points (0, 3, 6, 12, 24, and 48 h). As displayed in **Figure 6d**, brighter imaging intensity of MRI signals at the tumor site was observed after i.v. injection. The signal reached a maximum level at 12 h post-injection, which was supported by corresponding MRI signal intensity acquired from the Image J analysis (**Figure 6e**), confirming the efficient tumor accumulation of PHMZCO-AT nanozymes *via* the typical enhanced permeability and retention (EPR) effect.

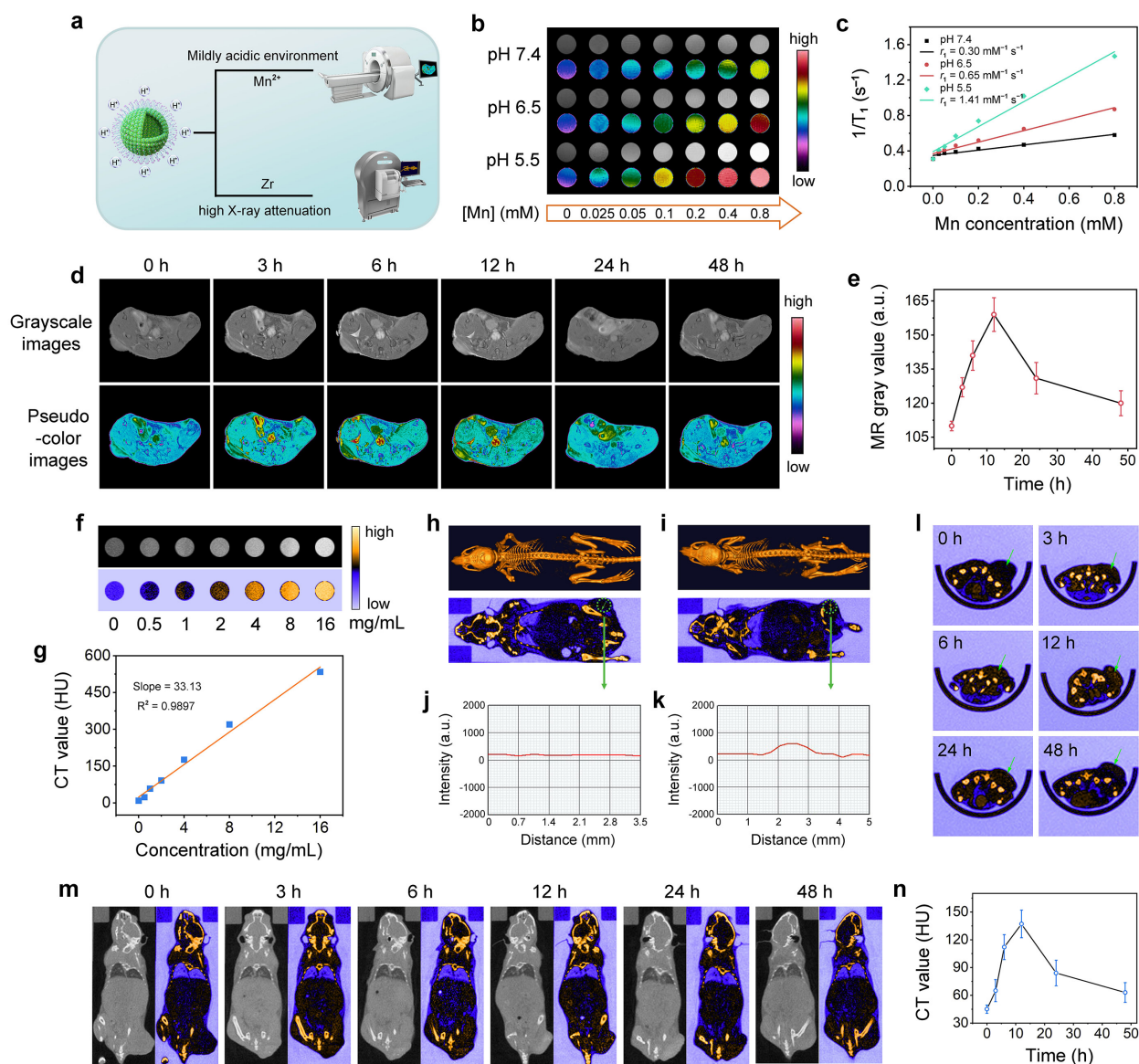


Figure 6. *In vitro* and *in vivo* MR and CT Imaging. (a) Schematic illustration of the pH-dependent T_1 -weighted MR imaging and Zr-enhanced CT imaging. (b) *In vitro* T_1 -MR images of PHMZCO-AT nanozymes with different concentrations (obtained under 9.4-T magnetic resonance scanner). (c) Relaxation rate r_1 versus Mn concentration of PHMZCO-AT nanozymes in different buffer solutions. (d) T_1 -weighted MR imaging of 4T1 tumor-bearing BALB/c mice intravenously injected with PHMZCO-AT nanozymes ([Mn] = 5 mg/kg) at various time points. (e) Corresponding MR

signal variations of the tumor region at detected time points analyzed by Image J software. (f) *In vitro* CT images of PHMZCO-AT nanozymes with different concentrations. (g) CT values *versus* different concentrations of PHMZCO-AT nanozymes. *In vivo* CT images of 4T1 tumor-bearing mice after intratumoral injection (h) without and (i) with PHMZCO-AT nanozyme solution (20 mg mL⁻¹), and (j,k) corresponding cross-sectional compositional line profiles of CT values. *In vivo* (l) transverse and (m) coronal sections of tumor region of 4T1 tumor-bearing mice after i.v. injection of PHMZCO-AT nanozyme solution at different time intervals. (n) Corresponding CT value variations of the tumor region measured by Image J software. Data are defined as mean \pm S.D. (n = 3).

It is well-known that CT imaging technology can afford deep tissue penetration and present detailed information of three-dimensional structures. The high X-ray attenuation ability of elemental Zr makes the PHMZCO-AT nanozymes a suitable CT imaging contrast agent.^[40] As seen from **Figure 6f**, the CT images are gradually brightened with the increase of PHMZCO-AT nanozymes. The Hounsfield unit (HU) value shows a positive linear relationship with the concentrations of PHMZCO-AT nanozymes, and the slope was calculated to be 33.13 (**Figure 6g**). The *in vivo* CT imaging was conducted on 4T1 tumor-bearing mice after intratumoral and i.v. injection of PHMZCO-AT nanozymes, respectively. As displayed in **Figure 6h** and **i**, remarkably enhanced CT signals were observed after intratumoral injection for 6 h as compared to pre-injection, as verified by corresponding cross-sectional CT line profiles (**Figure 6j** and **k**), suggesting the prolonged retention time of the nanozymes. When *in vivo* CT imaging was carried out on 4T1 tumor-bearing mice by i.v. injection of PHMZCO-AT nanozymes, CT images were acquired at 0, 3, 6, 12, 24, and 48 h post-injection by a small animal X-ray CT imaging system. The CT signal in the tumor site gradually increases with the brightest signal at 12 h post-injection, and visible CT signal is still visible even after 24 h post-injection (**Figure 6l** and **m**), as certified by the time-dependent variations in MRI signals measured by Image J software (**Figure 6n**). Both MRI and CT imaging results confirm the superiority of PHMZCO-AT nanozymes for real-time monitoring of tumor-homing ability of the nanozymes, thus providing precise guidance for NCDT.

Pharmacokinetics and *in Vivo* Intensive NCDT. The intriguing *in vitro* therapeutic efficacy of PHMZCO-AT nanozymes encouraged us to assess their anticancer performance *in vivo*. The therapeutic performance of PHMZCO-AT nanozymes was examined on 4T1 tumor xenograft on female BALB/c mice (**Figure 7a**). First, the pharmacokinetic profiles of the nanozymes were studied to illustrate their behavior *in vivo*. After the i.v. administration, the biodistribution of

PHMZCO-AT nanozymes at various time intervals was assessed (**Figure 7b**). The PHMZCO-AT nanozymes mainly accumulate in the spleen and liver owing to the capture by the reticuloendothelial system. The relative distribution amounts of PHMZCO-AT nanozymes in the tumor site were 3.2% ID g⁻¹ (percentage of injected dose per gram tissue) at 3 h post i.v. injection, 5.5% ID g⁻¹ at 6 h post i.v. injection, 7.1% ID g⁻¹ at 12 h post i.v. injection, 5.2% ID g⁻¹ at 24 h post i.v. injection, and 3.8% ID g⁻¹ at 48 h post i.v. injection, confirming that the PHMZCO-AT nanozymes can accumulate at tumor site by the EPR effect. In addition, the kidneys show obvious signals, illustrating that PHMZCO-AT nanozymes may be quickly eliminated through renal metabolism. As exhibited in **Figure 7c**, the blood circulation of PHMZCO-AT nanozymes follows a classic two-compartment model with moderate half-life times calculated to be $\tau_{1/2(\alpha)} = 0.15$ h and $\tau_{1/2(\beta)} = 4.93$ h, which would be beneficial for high tumor accumulation.^[41]

Then, after the tumor volume reached nearly 30 mm³, twenty-five 4T1 tumor-bearing BALB/c mice were randomly divided into five groups (n = 5 per group): (1) control (saline), (2) free 3-AT, (3) CeO₂, (4) HMZCO, and (5) PHMZCO-AT. The samples from each group were treated by i.v. injection on days 1, 7, and 14. The injection doses of different samples were 15 mg/kg mouse body weight. The tumor volume and body weight of each mouse were recorded every two days during the therapeutic process. As displayed in **Figure 7d**, the tumor progression in mice injected with PHMZCO-AT nanozymes was remarkably restrained in comparison with other groups. To be more specific, the suppression rate of the PHMZCO-AT-treated group was determined to be 81.9%, calculated by the variation of the relative tumor volume. The suppression is attributed to the PHMZCO-AT-mediated cascade catalytic reaction as follows: (1) the PHMZCO-AT nanozymes can convert endogenous O₂^{•-} into H₂O₂, and inhibit the off-target depletion of H₂O₂; (2) the disruption of the H₂O₂ homeostasis in cancer cells by the PHMZCO-AT nanozymes achieves a high accumulation of H₂O₂; (3) the elevated H₂O₂ can be exclusively catalyzed by the downstream POD-like activity of PHMZCO-AT nanozymes to generate abundant toxic ·OH for achieving intensive NCDT.

Such an excellent antitumor efficacy was affirmed by analyzing excised tumor weight and corresponding visualized photographs (**Figure 7e**). The body weights of mice in therapeutic and control groups display no obvious variations during 20 days of the therapeutic process (**Figure 7f**), indicating that there is no acute toxicity during the treatment. In addition, the PHMZCO-AT group remarkably prolongs the survival time of tumor-bearing mice as compared with other treatment groups after 40 days (**Figure 7g**). The intensive NCDT efficacy was also confirmed by hematoxylin and eosin (H&E) staining and TdT-mediated dUTP nick-end labeling (TUNEL) staining of tumor sections from each group (**Figure 7h**). Consistent with the tumor growth data, the PHMZCO-AT

group shows the most severe tumor damage and condensed nuclei of cancer cells when compared with the other four groups. Additionally, the hemolysis analysis, biochemical blood analysis, routine examination, and H&E staining images of major organs after the whole treatment period indicate that the PHMZCO-AT nanozymes possess good *in vivo* biocompatibility (Figure S25-S28).

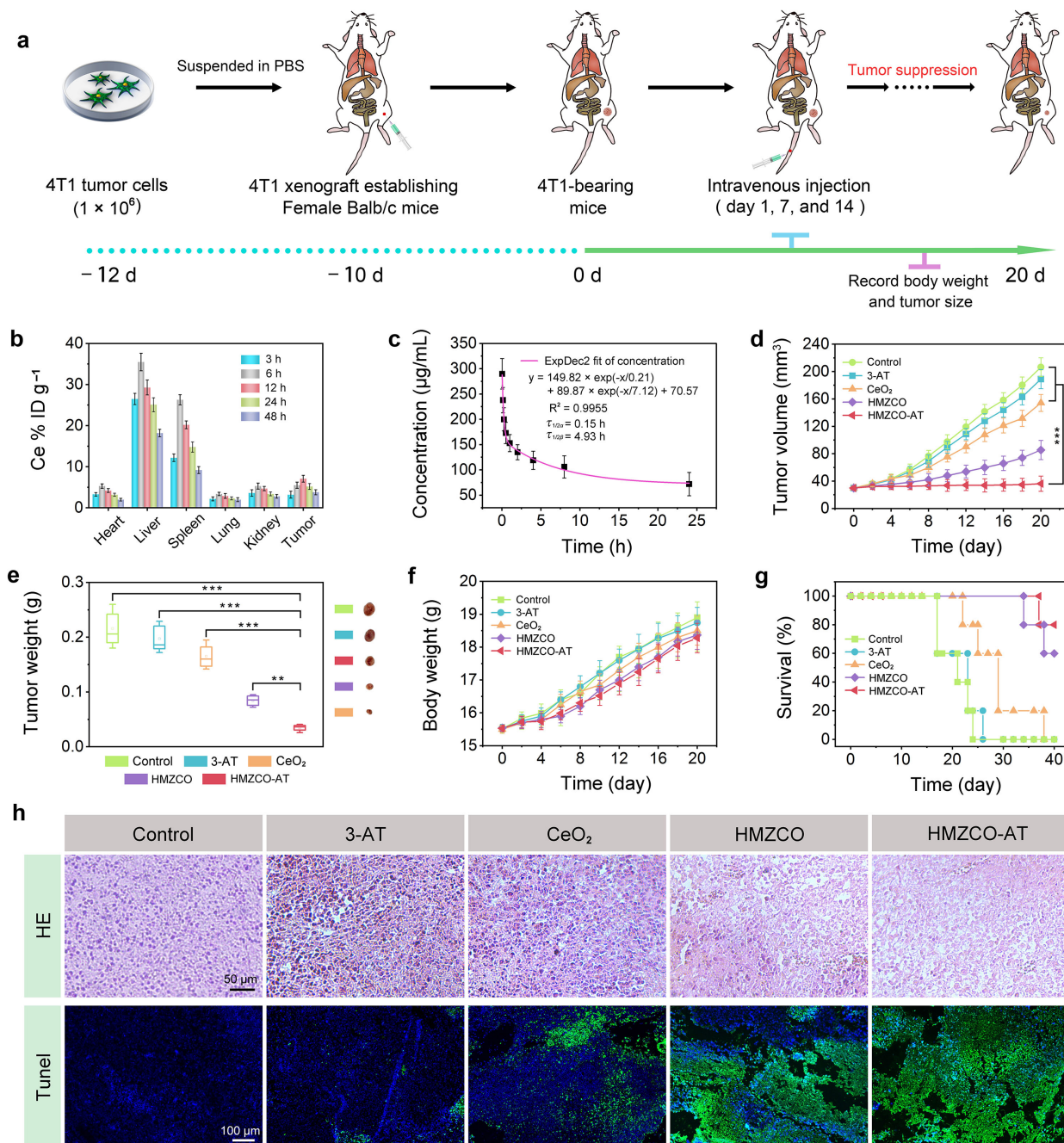


Figure 7. Pharmacokinetic evaluation and *in vivo* NCDT efficiency assessments. (a) Schematic diagram showing the establishment of the 4T1 tumor xenograft tumor model and treatment regimen. (b) Biodistribution of PHMZCO-AT nanozymes in main organs and tumors at different time points ($n = 3$). (c) Blood circulation curve of intravenously injected PHMZCO-AT nanozymes. Data are expressed as mean \pm S.D. ($n = 3$). (d) Tumor volume and (e) tumor weight changes (right panel:

representative images of the dissected tumors from each tumor group at day 20) of 4T1 tumor-bearing mice with different treatments. Data are expressed as mean \pm S.D. (n = 5). Statistical significance is assessed by unpaired Student's two-sided *t* test, ***P* < 0.005, ****P* < 0.001. (f) Body weight changes of 4T1 tumor-bearing mice in the treatment process (n = 5). (g) Survival percentage of tumor-bearing nude mice after different treatments (n = 5). (h) H&E and TUNEL-stained photographs of tumor slices obtained from tumor-bearing mice treated with various treatments after 20 days.

Conclusions

In summary, a “broadening source and reducing the off-target expenditure of H₂O₂” strategy has been introduced into the hollow cerium-based tandem nanozyme (PHMZCO-AT) to significantly disturb H₂O₂ homeostasis by elaborately regulating multi-enzymatic activities for intensive NCDT. With superior SOD-like activity, restrained CAT-like activity, and GSH-depletion capacity, the PHMZCO nanozymes can accelerate the generation and restrain the off-target elimination of H₂O₂ with the assistance of 3-AT-inhibited endogenous CAT activity, leading to the rapid increase of the H₂O₂ level in cancer cells. The elevated H₂O₂ is then exclusively and continuously catalyzed by the downstream POD-like activity of PHMZCO-AT nanozymes to liberate highly abundant \cdot OH through the Fenton-like reaction, consequently inducing apoptotic cell death both *in vitro* and *in vivo*. Meanwhile, the enzymatic catalytic activity of PHMZCO-AT nanozymes has been evaluated in detail according to the Michaelis–Menten steady-state kinetics. In addition, tumor-responsive contrast-enhanced *T*₁-MRI and CT imaging have been achieved owing to the existence of the paramagnetic Mn²⁺ species and the high X-ray attenuation ability of elemental Zr in PHMZCO-AT, permitting *in vivo* monitoring of the therapeutic process. By combining dual-mode imaging and pharmacokinetic analysis, PHMZCO-AT nanozymes possess efficient tumor-homing capability at 12 h post i.v. injection. Notably, the PHMZCO-AT nanozymes exhibit a superior tumor-suppression effect on 4T1 tumor xenograft (81.9%) guided by the designed treatment protocols. Thus, the PHMZCO-AT tandem nanozyme presents a general paradigm for facile construction of advanced nanozymes with elaborately regulated multi-enzymatic activities toward efficient tumor-catalytic therapy.

Supporting Information

Supporting Information is available from the Wiley Online Library or from the author.

Acknowledgements

The work was supported by the MOST Grant (2016YFA0101202), the National Natural Science Foundation of China (51972075 and 51772059), the Singapore Agency for Science, Technology and Research (A*STAR) AME IRG grant (A20E5c0081), and the Singapore National Research Foundation Investigatorship (NRF-NRFI2018-03). The authors thank Dr. Jianwei Su and Dr. Peng Jiang for kind help and valuable suggestions. All animal experiments were approved by the Ethics Committee of the Second Affiliated Hospital of Harbin Medical University (Harbin, China). The procedure of animal experiments was performed under the Guidelines for Care and Use of Laboratory Animals of the Drug Safety Evaluation Center of Harbin Medical University (No. SYDW 2019-82).

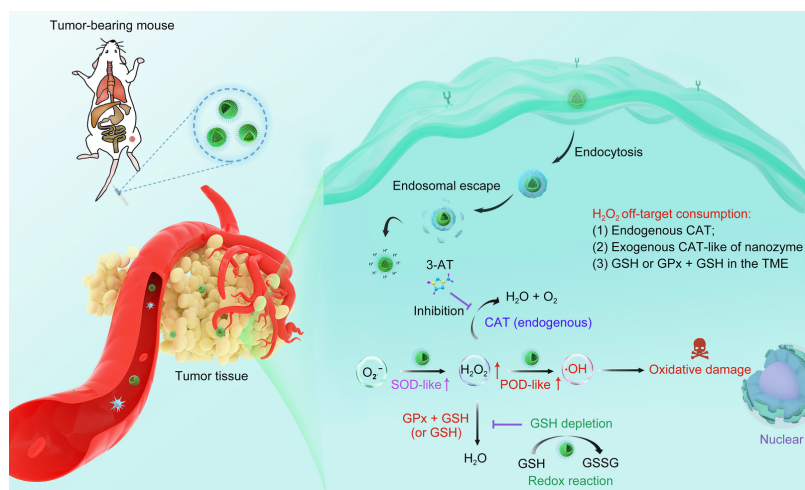
References

- [1] a) B. Yang, Y. Chen, J. Shi, *Chem. Rev.* **2019**, *119*, 4881; b) R. A. Cairns, I. S. Harris, T. W. Mak, *Nat. Rev. Cancer* **2011**, *11*, 85; c) D. Trachootham, J. Alexandre, P. Huang, *Nat. Rev. Drug Discovery* **2009**, *8*, 579.
- [2] a) D. Wang, H. Wu, G. Yang, C. Qian, L. Gu, H. Wang, W. Zhou, J. Liu, Y. Wu, X. Zhang, Z. Guo, H. Chen, D. Jana, Y. Zhao, *ACS Nano* **2020**, *14*, 13500; b) J.-J. Hu, Q. Lei, X.-Z. Zhang, *Prog. Mater. Sci.* **2020**, *114*, 100685.
- [3] a) C. Sandhya, M. C. Jared, D. Wei, G. Anna, N. Saadia, L. Guozhen, C. W. Brian, M. G. Ewa, *Adv. Sci.* **2020**, *7*, 2003584; b) Y. Wu, L. Su, M. Yuan, T. Chen, J. Ye, Y. Jiang, J. Song, H. Yang, *Angew. Chem., Int. Ed.* **2021**, *60*, 12868.
- [4] a) S. Liang, X. Deng, P. a. Ma, Z. Cheng, J. Lin, *Adv. Mater.* **2020**, *32*, 2003214; b) X. Lin, S. Liu, X. Zhang, R. Zhu, S. Chen, X. Chen, J. Song, H. Yang, *Angew. Chem., Int. Ed.* **2020**, *59*, 1682.
- [5] a) G. Liu, J. Zhu, H. Guo, A. Sun, P. Chen, L. Xi, W. Huang, X. Song, X. Dong, *Angew. Chem., Int. Ed.* **2019**, *58*, 18641; b) Z. Tang, P. Zhao, H. Wang, Y. Liu, W. Bu, *Chem. Rev.* **2021**, *121*, 1981.
- [6] a) F. Liu, L. Lin, Y. Zhang, Y. Wang, S. Sheng, C. Xu, H. Tian, X. Chen, *Adv. Mater.* **2019**, *31*, 1902885; b) K. Fan, J. Xi, L. Fan, P. Wang, C. Zhu, Y. Tang, X. Xu, M. Liang, B. Jiang, X. Yan, L. Gao, *Nat. Commun.* **2018**, *9*, 1440.
- [7] a) S. M. Dong, Y. S. Dong, T. Jia, F. M. Zhang, Z. Wang, L. L. Feng, Q. Q. Sun, S. L. Gai, P. Yang, *Chem. Mater.* **2020**, *32*, 9868; b) M. Huo, L. Wang, Y. Chen, J. Shi, *Nat. Commun.* **2017**, *8*, 357.
- [8] a) R. André, F. Natálio, M. Humanes, J. Leppin, K. Heinze, R. Wever, H. C. Schröder, W. E. G. Müller, W. Tremel, *Adv. Funct. Mater.* **2011**, *21*, 501; b) L. Han, L. Zeng, M. Wei, C. M. Li, A. Liu, *Nanoscale* **2015**, *7*, 11678.

- [9] A. P. Nagvenkar, A. Gedanken, *ACS Appl. Mater. Interfaces* **2016**, *8*, 22301.
- [10] a) S. Dong, Y. Dong, T. Jia, S. Liu, J. Liu, D. Yang, F. He, S. Gai, P. Yang, J. Lin, *Adv. Mater.* **2020**, *32*, 2002439; b) C. Liu, M. Zhang, H. Geng, P. Zhang, Z. Zheng, Y. Zhou, W. He, *Appl. Catal., B* **2021**, *295*, 120317.
- [11] X. Liu, D. Huang, C. Lai, L. Qin, G. Zeng, P. Xu, B. Li, H. Yi, M. Zhang, *Small* **2019**, *15*, 1900133.
- [12] L. Zhang, S. S. Wan, C. X. Li, L. Xu, H. Cheng, X. Z. Zhang, *Nano Lett.* **2018**, *18*, 7609.
- [13] a) Z. Tang, Y. Liu, M. He, W. Bu, *Angew. Chem., Int. Ed.* **2019**, *58*, 946; b) Y. Dai, C. Xu, X. Sun, X. Chen, *Chem. Soc. Rev.* **2017**, *46*, 3830.
- [14] a) S. M. Jo, F. R. Wurm, K. Landfester, *Nano Lett.* **2020**, *20*, 526; b) C. Liu, Y. Cao, Y. Cheng, D. Wang, T. Xu, L. Su, X. Zhang, H. Dong, *Nat. Commun.* **2020**, *11*, 1735.
- [15] Laura A. Sena, Navdeep S. Chandel, *Mol. Cell* **2012**, *48*, 158.
- [16] a) W. Zhang, S. Hu, J.-J. Yin, W. He, W. Lu, M. Ma, N. Gu, Y. Zhang, *J. Am. Chem. Soc.* **2016**, *138*, 5860; b) W. Feng, X. Han, H. Hu, M. Chang, L. Ding, H. Xiang, Y. Chen, Y. Li, *Nat. Commun.* **2021**, *12*, 2203.
- [17] a) C. Yao, W. Wang, P. Wang, M. Zhao, X. Li, F. Zhang, *Adv. Mater.* **2018**, *30*, 1704833; b) E. G. Heckert, A. S. Karakoti, S. Seal, W. T. Self, *Biomaterials* **2008**, *29*, 2705; c) Z. Tian, H. Liu, Z. Guo, W. Gou, Z. Liang, Y. Qu, L. Han, L. Liu, *Small* **2020**, *16*, 2004654.
- [18] V. Baldim, F. Bedioui, N. Mignet, I. Margaill, J. F. Berret, *Nanoscale* **2018**, *10*, 6971.
- [19] C. Xu, X. Qu, *NPG Asia Mater.* **2014**, *6*, e90.
- [20] Y. Yang, Z. Mao, W. Huang, L. Liu, J. Li, J. Li, Q. Wu, *Sci. Rep.* **2016**, *6*, 35344.
- [21] a) L. Alili, M. Sack, A. S. Karakoti, S. Teuber, K. Puschmann, S. M. Hirst, C. M. Reilly, K. Zanger, W. Stahl, S. Das, S. Seal, P. Brenneisen, *Biomaterials* **2011**, *32*, 2918; b) S. Singh, T. Dosani, A. S. Karakoti, A. Kumar, S. Seal, W. T. Self, *Biomaterials* **2011**, *32*, 6745.
- [22] a) Y. Auyeung, R. E. Sievers, D. Weng, V. Barbosa, C. L. Wolfe, *Circulation* **1995**, *92*, 3318; b) A. Coto-Montes, R. Hardeland, *J. Pineal Res.* **1999**, *27*, 154.
- [23] X. Liang, X. Wang, Y. Zhuang, B. Xu, S. Kuang, Y. Li, *J. Am. Chem. Soc.* **2008**, *130*, 2736.
- [24] V. Perala, N. R. Komateedi, J. Deshetti, M. R. Benjaram, *Appl. Catal., B* **2015**, *162*, 122.
- [25] W. Liu, X. Liu, L. Feng, J. Guo, A. Xie, S. Wang, J. Zhang, Y. Yang, *Nanoscale* **2014**, *6*, 10693.
- [26] B. A. Reddy, A. Khan, Y. Yamada, T. Kobayashi, S. Lorient, J. C. Volta, *J. Phys. Chem. B* **2002**, *106*, 10964.
- [27] H. T. Li, Q. Gao, G. S. Wang, B. Han, K. S. Xia, C. H. Zhou, *Appl. Surf. Sci.* **2020**, *502*, 144295.

- [28] a) M. Yan, T. Mori, J. Zou, F. Ye, D. R. Ou, J. Drennan, *Acta Mater.* **2009**, *57*, 722; b) Y. Lykhach, S. M. Kozlov, T. Skála, A. Tovt, V. Stetsovych, N. Tsud, F. Dvořák, V. Johánek, A. Neitzel, J. Mysliveček, S. Fabris, V. Matolín, K. M. Neyman, J. Libuda, *Nat. Mater.* **2016**, *15*, 284.
- [29] Y. Sang, F. Cao, W. Li, L. Zhang, Y. You, Q. Deng, K. Dong, J. Ren, X. Qu, *J. Am. Chem. Soc.* **2020**, *142*, 5177.
- [30] B. Jiang, D. Duan, L. Gao, M. Zhou, K. Fan, Y. Tang, J. Xi, Y. Bi, Z. Tong, G. F. Gao, N. Xie, A. Tang, G. Nie, M. Liang, X. Yan, *Nat. Nanotechnol.* **2018**, *13*, 1506.
- [31] S. Ji, B. Jiang, H. Hao, Y. Chen, J. Dong, Y. Mao, Z. Zhang, R. Gao, W. Chen, R. Zhang, Q. Liang, H. Li, S. Liu, Y. Wang, Q. Zhang, L. Gu, D. Duan, M. Liang, D. Wang, X. Yan, Y. Li, *Nat. Catal.* **2021**, *4*, 407.
- [32] B. Yu, W. Wang, W. Sun, C. Jiang, L. Lu, *J. Am. Chem. Soc.* **2021**, *143*, 8855.
- [33] Z. Wang, X. Shen, X. Gao, Y. Zhao, *Nanoscale* **2019**, *11*, 13289.
- [34] Z. Tan, J. Zhang, Y.-C. Chen, J.-P. Chou, Y.-K. Peng, *J. Phys. Chem. Lett.* **2020**, *11*, 5390.
- [35] a) J. Chen, J. Li, J. Zhou, Z. Lin, F. Cavalieri, E. Czuba-Wojnilowicz, Y. Hu, A. Glab, Y. Ju, J. J. Richardson, F. Caruso, *ACS Nano* **2019**, *13*, 11653; b) R. V. Benjaminsen, M. A. Matthebjerg, J. R. Henriksen, S. M. Moghimi, T. L. Andresen, *Mol. Ther.* **2013**, *21*, 149.
- [36] X. Lu, S. Gao, H. Lin, L. Yu, Y. Han, P. Zhu, W. Bao, H. Yao, Y. Chen, J. Shi, *Adv. Mater.* **2020**, *32*, 2002246.
- [37] W. Zhen, Y. Liu, W. Wang, M. Zhang, W. Hu, X. Jia, C. Wang, X. Jiang, *Angew. Chem., Int. Ed.* **2020**, *59*, 9491.
- [38] Y. Chen, Z.-H. Li, J.-J. Hu, S.-Y. Peng, L. Rong, Y. Sun, X.-Z. Zhang, *Nanoscale Horiz.* **2019**, *5*, 283.
- [39] a) X. Qian, X. Han, L. Yu, T. Xu, Y. Chen, *Adv. Funct. Mater.* **2020**, *30*, 1907066; b) X. Pan, W. Wang, Z. Huang, S. Liu, J. Guo, F. Zhang, H. Yuan, X. Li, F. Liu, H. Liu, *Angew. Chem., Int. Ed.* **2020**, *59*, 13557.
- [40] Z. Chen, M. Niu, G. Chen, Q. Wu, L. Tan, C. Fu, X. Ren, H. Zhong, K. Xu, X. Meng, *ACS Nano* **2018**, *12*, 12721.
- [41] C.-C. Xue, M.-H. Li, Y. Zhao, J. Zhou, Y. Hu, K.-Y. Cai, Y. Zhao, S.-H. Yu, Z. Luo, *Sci. Adv.* **2020**, *6*, eaax1346.

Table of Contents Graphic



A hollow mesoporous Mn/Zr-co-doped CeO_2 tandem nanozyme is developed, serving as an H_2O_2 homeostasis disruptor to promote H_2O_2 evolvement, restrain the off-target elimination of H_2O_2 , and exclusively catalyze by the downstream peroxidase-like activity for achieving intensive nanozyme-initiated chemodynamic therapy of tumor. T_1 -weighted magnetic resonance imaging and high-contrast X-ray computed tomography imaging are also achieved using the nanozyme for *in vivo* tracking of the therapeutic process.